nature physics

Article

https://doi.org/10.1038/s41567-023-02202-4

Evidence of finite-momentum pairing in a centrosymmetric bilayer

Received: 14 June 2022

Accepted: 3 August 2023

Published online: 4 September 2023

Check for updates

Dong Zhao, Lukas Debbeler, Matthias Kühne, Sven Fecher, Nils Gross & Jurgen Smet

A phase characterized by a spatially modulated order parameter is counter-intuitive because of the entropy penalty that the modulations incur. Its possible existence in superconductors was first proposed under the condition that the formation of Cooper pairs is limited to some segments of the Fermi surface and that the Cooper pairs carry momentum above the Pauli limit. This prediction motivated experimental efforts to identify such non-uniform superconducting states in organic superconductors, heavy fermion compounds and cuprates. Here we report evidence of another type of finite-momentum pairing that manifests below the Pauli limit. It is driven by the orbital effect and does not rely on Fermi surface segmentation. We have evidence of this spatially modulated superconducting state in a hexagonal MoS_2 bilayer through remote intercalation that offers both balanced doping and firm out-of-plane coherence across both layers.

In the classic Bardeen–Cooper–Schrieffer (BCS) theory for conventional superconductors, Cooper pairs carry no momentum, and the gap, which forbids a current of unpaired electrons to flow, is spatially uniform within the condensate, guaranteeing zero current in the ground state. A decade later, Fulde and Ferrell[1] and Larkin and Ovchinnikov[2] predicted that under appropriate conditions, a non-uniform ground state may supplant the BCS state at high magnetic field and low temperature. This state is composed of Cooper pairs that carry finite momentum and are formed only from some segments of the Fermi surface (Fig. 1a). Concomitantly, the order parameter is spatially modulated such that the total current remains zero. The most plausible experimental evidence for this Fulde–Ferrell–Larkin–Ovchinnikov (FFLO) state was found in quasi-two-dimensional (2D) organic superconductors[3–5]. Research has reported other generic non-uniform superconducting states in various systems. These include the helical state in non-centrosymmetric superconductors[6,7], the Q-phase in heavy fermion compounds[8,9] and the pair density wave state in the cuprates[10] and transition-metal dichalcogenides[11]. In these non-uniform states, it is a deformation of the Fermi surface that promotes the appearance of momentum-carrying Cooper pairs along certain segments of the Fermi surface. In the absence of inversion symmetry, this deformation can originate from the Rashba or Dresselhaus spin–orbit coupling (SOC). Also magnetic orders, such as those that appear in heavy fermion compounds and cuprates, can cause such a deformation of the Fermi surfaces.

Recently, a new type of finite-momentum pairing was predicted in centrosymmetric layered materials with Ising SOC[12]. In contrast to previously reported non-uniform states, the entire Fermi surface can be gapped and is not necessarily segmented or deformed. Paradoxically, the participation of the full Fermi surface is stimulated by the orbital effect, that is the overall shift of the Fermi surface in momentum space as carriers gain field momentum (Fig. 1b), although this effect is normally detrimental for finite-momentum pairing. It has been the primary reason that heavy fermion systems and 2D superconductors have been preferred choices in the search for non-uniform superconducting states. To host this novel state, the material must fulfil two prerequisites. First, the carrier population should inherit an out-of-plane spin texture through the band structure with the spin polarity locked to both the momentum and layer degrees of freedom. This is a special case of the hidden spin polarization in layered materials with SOC[13–15]. It requires that the layer sector is mirror symmetric but non-centrosymmetric, whereas the material as a whole is centrosymmetric. Second, superconductivity should be layer-coherent, such that pairing channels inherit the symmetry of the global system. Layered superconductors with the required symmetries are not rare; they can be found among the transition-metal dichalcogenides. Typically, however, the effective out-of-plane coherence length is well below the layer spacing at low temperature[16–22]. Consequently, gaps among different layers are decoherent and the gap symmetry is determined by

Max Planck Institute for Solid State Research, Stuttgart, Germany. e-mail: j.smet@fkf.mpg.de

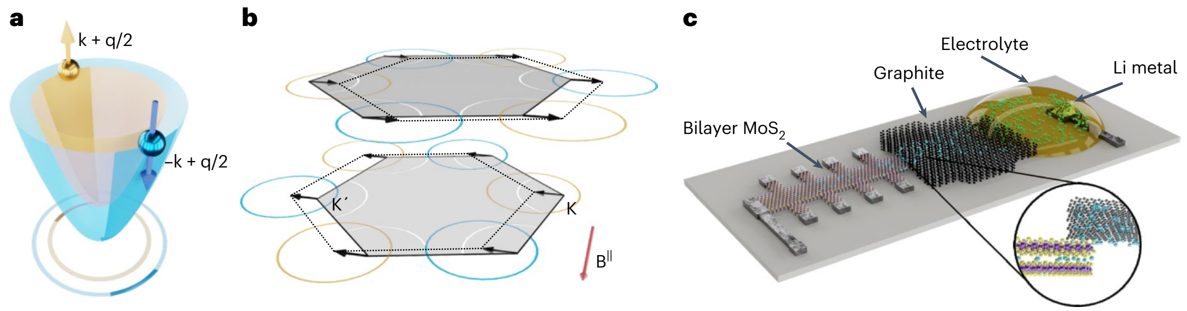

Fig. 1 | Instances of finite-momentum pairing and sample configuration. **a**, Segmented Fermi surface for finite-momentum pairing of electrons in an FFLO state. Pairing only occurs for the darker coloured segments of the Fermi surface. **b**, Finite-momentum pairing in bilayer MoS$_2$, where the complete Fermi surface participates in pairing. Due to the Ising SOC, the bands centred around K and K' with the lowest energy states have opposite spin. Only these bands with the lowest energy states are shown. They are all shifted by an identical field momentum as a result of the applied in-plane magnetic field, but in opposite direction for the top and bottom layer. **c**, Schematic of the device geometry consisting of a 2H-MoS$_2$ bilayer. A graphene multilayer, whose van der Waals galleries get electrochemically filled with lithium using the galvanic cell on the right, acts as a conveyor to transport lithium from the electrolyte drop to the single MoS$_2$ van der Waals gallery. The inset illustrates the diffusion of lithium all the way into MoS$_2$.

the layer sector only, preventing the observation of this new state. In the absence of layer coherence, Ising pairing, expected in monolayers, is favoured instead. It accounts for the excessively high in-plane upper critical field in, for instance, multilayer NbSe$_2$ (ref. 20), TaS$_2$ (ref. 21) and MoS$_2$ electric double-layer transistors (EDLTs)[23,24]. Also, the use of the potent ionic liquid gating technique to induce a sufficiently high density promotes Ising pairing in multilayer samples, since charge carriers primarily accumulate in the topmost layer only, and the liquid coverage of the active area is prone to add disorder, which has an adverse effect on the effective out-of-plane coherence length.

Here, we attempt to provide the missing prerequisite of out-of-plane coherence across the entire film in a 2H-MoS$_2$ bilayer with D_{3d} symmetry. We assume that the conduction band minima are located at the K- and K'-symmetry points (Supplementary Section 2). The mirror symmetry and absence of inversion symmetry within each layer lift the spin degeneracy to produce an out-of-plane spin texture with opposite polarity for the K- and K'-valleys and for equivalent valleys of the two layers. Hence, the spin, valley and layer degrees are locked[13–15]. A state-of-the-art device-level remote intercalation technique has been deployed. It enables to reversibly dope the MoS$_2$ bilayer in a balanced fashion through charge transfer from lithium intercalants and preserves centrosymmetry. The device geometry is illustrated in Fig. 1c. A graphene multilayer acts as a conveyor to transfer the lithium from the electrolyte to the van der Waals gallery of the MoS$_2$ bilayer with the help of a peripheral galvanic cell developed in refs. 25,26 (see description in Methods). The intercalants are inserted in the single van der Waals gallery along a small portion of the sample perimeter with no need for liquid coverage of the active device area, which is far more invasive. Figure 2a plots the temperature dependence of the sheet resistance R_{s} of three different samples with varying carrier density achieved through remote lithium intercalation. The mean-field superconducting transition temperature T_{c0} at which the amplitude of the gap function becomes non-zero was taken as $T_{0.5R_{\mathrm{N}}}$, that is, at half height of the normal-state resistance R_{N}. The onset temperature for phase coherence of the gap function is the Berezinskii–Kosterlitz–Thouless transition temperature T_{BKT}, and is obtained from an analysis of temperature-dependent I–V characteristics (Supplementary Section 3). It closely agrees with T_{c0} as anticipated for low-disorder thin films with $R_{\mathrm{N}} \ll h/4e^2$ (refs. 20,27), where h is the Planck constant and e is the elementary charge. The density dependence of the T_{c0} is plotted in Fig. 2b for five different samples. The carrier density per layer, calculated by dividing the measured Hall density by the layer degeneracy, serves as the abscissa and is denoted as n_{s}. Figure 2 also includes data from the literature measured on single-side EDLTs[28], double-side gated EDLT bilayers[22] and chemically intercalated bulk MoS$_2$ (ref. 18). In the single-side EDLTs, the assumption is that charges accumulate in the topmost layer. For the bulk MoS$_2$, n_{s} is calculated from the nominal stoichiometry following ref. 28. While lithium intercalation is the primary source of doping in our samples, it is possible to fine-tune the density in a limited range by using the doped silicon substrate as a backgate. This offers the opportunity to fit the density-dependent transition temperature to the scaling law $T_{\mathrm{c0}} \propto (n_{\mathrm{s}} - n_{\mathrm{Q}})^{z\nu}$ with the critical exponents z and ν and the density n_{Q} at the quantum critical point of the superconducting transition at temperature $T = 0$ (ref. 28). We obtain $z\nu \approx 0.6$ and $n_{\mathrm{Q}} = 3.74 \times 10^{13}\ \mathrm{cm}^{-2}$ (inset to Fig. 2b). The latter is about half of that reported for MoS$_2$ in the EDLT configuration[28]. All of our MoS$_2$ samples exhibit superconductivity at unprecedented low densities, and the data generate a mini-dome adjacent to the previously reported superconducting dome in the T_{c0}–n_{s} diagram of MoS$_2$ (Fig. 2b) suggesting that the use of the unconventional sample design (Fig. 1c) has enabled the disclosure of a previously inaccessible regime of superconductivity. This is also corroborated by a comparison of key length scales, such as the mean free path l_{mfp} and the zero-temperature in-plane ($\xi^{\|}$) and out-of-plane ($\xi^{\perp}$) coherence lengths determined from a three-dimensional Ginzburg–Landau model (Supplementary Section 5) for samples exhibiting superconductivity within and outside of this mini-dome. Figure 2c summarizes the values for these lengths obtained in our samples. For comparison, the values for data reported in ref. 22 on double-side gated MoS$_2$ bilayers belonging to the adjacent superconducting dome have also been included. Particularly noteworthy is the zero-temperature out-of-plane coherence length comparable to the sample thickness in our devices, a crucial prerequisite for hosting the orbital-effect-driven finite-momentum pairing scheme[12].

To assess the nature of superconductivity, it is instrumental to study the robustness of pairing against an in-plane magnetic field and use the upper critical field expected for a conventional BCS thin-film superconductor with the same sample thickness d as the benchmark. In a BCS superconductor, pair breaking is initiated by preferential orientation of the spin magnetic moment induced by the Zeeman effect or by the orbital magnetic moment originating from the cyclotron motion. The Zeeman effect causes pair breaking when the Zeeman splitting becomes comparable to the gap amplitude, which imposes a critical field $B_{\mathrm{P}} = 1.85 T_{\mathrm{c0}}$ in the zero-temperature limit, referred to as the Pauli limit. The orbital effect manifests when the energy difference between electrons of opposite wavevector $\mathbf{k}$ becomes comparable to the gap amplitude, that is $\langle |E(\mathbf{k} + \mathbf{q}_{B^{\|}}) - E(-\mathbf{k} + \mathbf{q}_{B^{\|}})| \rangle_{\mathrm{F}} \approx \Delta$, where E is the kinetic energy, $\langle \ldots \rangle_{\mathrm{F}}$ denotes the average over the Fermi surface and $\mathbf{q}_{B^{\|}}$ corresponds to the field momentum $\hbar \mathbf{q}_{B^{\|}} = e\mathbf{A}$ for vector potential $\mathbf{A}$. For the in-plane field $\mathbf{B}^{\|}$, the gauge $\mathbf{A} = \mathbf{B}^{\|} \times \mathbf{z}$ was chosen with the sample surface normal along $\mathbf{z}$ and with $z = \pm d/2$ for the upper

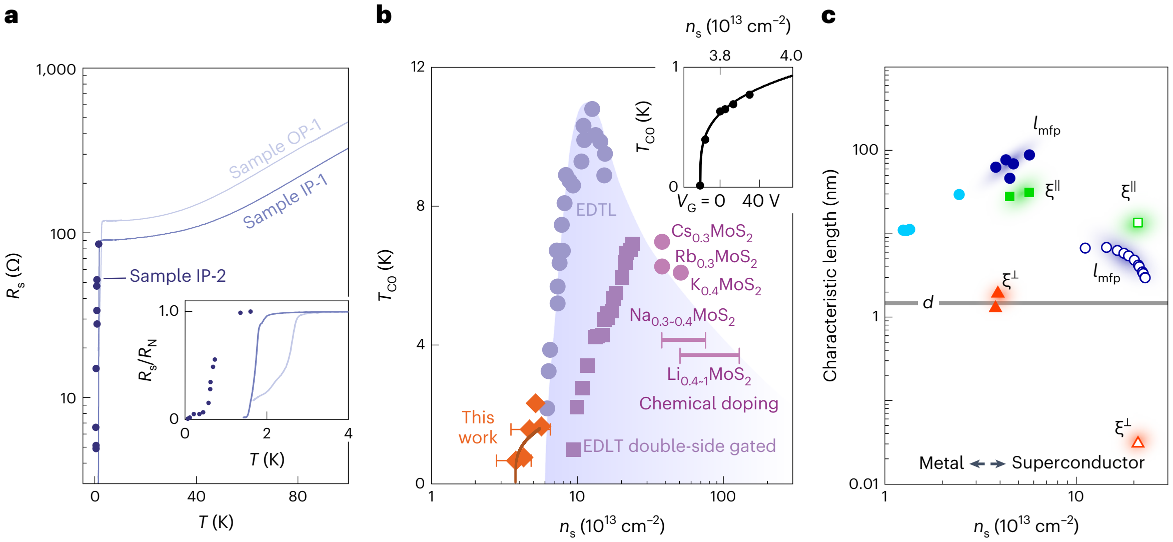

Fig. 2 | Superconductivity in a lithium intercalated 2H-MoS$_2$ bilayer and characteristic length scales. **a**, Temperature dependence of R_s obtained on three different samples. Sample IP-2 was measured in a dilution refrigerator to be able to record data (the circles) down to 50 mK. The inset displays magnified detail near the superconducting transition. **b**, Dependence of the critical temperature on the carrier density per layer. In this work, data points were obtained on a total of five samples (OP-1, OP-2, OP-3, IP-1 and IP-2). Error bars reflect the carrier density variation due to the density gradient along the Hall bar (Supplementary Section 2). Data from literature on bulk chemically doped samples and single- and double-sided EDLTs in refs. [22,28] are included as well. The inset shows density-dependent data for sample IP-2 together with a fit to the scaling law $T_{C0} \propto (n_s - n_Q)^{z\nu}$ (see also ref. [28]). V_G refers here to the backgate voltage. **c**, The mean free path (l_{mfp}, circles), the zero-temperature out-of-plane ($\xi^{\perp}$, red triangles) and in-plane ($\xi^{\parallel}$, green squares) coherence lengths extracted from one metallic sample M-1 (light-blue solid circles) and five superconducting samples (OP-1, OP-2, OP-3, IP-1 and IP-2) (dark-blue solid circles). Hollow symbols are the characteristic lengths previously reported in the literature for double-side gated bilayers in ref. [22]. Colour-shaded areas are visual guides. The grey line marks the thickness, d, of the bilayer.

and lower layer[12,29]. When assuming a parabolic energy dispersion, integrating over a circular Fermi surface and substituting the universal formula for the temperature dependence of the BCS gap, $\Delta(T) = 1.76 k_B T_{C0} \tanh(1.74\sqrt{T_{C0}/T - 1})$, we obtain an upper critical field, $B^{\parallel}_{c2}$, imposed by the orbital effect equal to

$$B^{\parallel}_{c2} = B_{orb} \tanh(1.74\sqrt{T_{C0}/T - 1}). \qquad (1)$$

Here, k_B is the Boltzmann constant and $B_{orb} = 0.88\pi k_B T_{C0}/(ed\upsilon_F)$ is the orbital-effect limit of $B^{\parallel}_{c2}$ at $T = 0$; it is density dependent via the Fermi velocity υ_F (Supplementary Section 2). The orbital-effect limit can also be determined from the flux penetrating the region enclosed by the sample thickness and the BCS coherence length $\hbar\upsilon_F/(\pi\Delta)$[30]. This yields a similar expression. With a film thickness $d = 1.8$ nm and a Fermi velocity in the range of 3.1–3.6×10^5 m s^{-1} for the densities accessed in this work, B_{orb} is between $0.36T_{C0}$ and $0.42T_{C0}$. This field is several times lower than the Pauli limit. Hence, if the two layers are coherent, the orbital effect will set the pair-breaking limit.

The temperature dependence of $B^{\parallel}_{c2}$ recorded on three of our samples is plotted in Fig. 3a and Extended Data Fig. 1. The temperature is normalized to T_{C0} to enable a comparison among different samples. $B^{\parallel}_{c2}$ is normalized to B_{orb}. For one sample, similar data have been acquired with the backgate voltage as an additional control for tuning the carrier density (Fig. 3b). In all cases a characteristic dimensionless temperature $t_c \approx 0.9$ can be identified that separates two regimes with distinct T dependencies. For $T/T_{C0} > t_c$, the T-dependence of $B^{\parallel}_{c2}$ follows equation (1) and $B^{\parallel}_{c2}$ approaches B_{orb} as $T \to 0$. The critical temperature for the different samples in Fig. 3a and densities in Fig. 3b varies from 0.38 K to 1.63 K, yet the agreement with equation (1) is excellent and sample-invariant. The limit imposed by the Zeeman effect is included in Fig. 3c for comparison, but is clearly irrelevant in this temperature regime. This indicates that for $T/T_{C0} > t_c$, the MoS$_2$ bilayer is in a conventional BCS state where the pairing stability is limited by the orbital effect and the two layers are coherent. For $T/T_{C0} < t_c$, this universality is lost; curves no longer follow equation (1) and the behaviour becomes both sample- and density-dependent (cf. Fig. 3a and Fig. 3b, respectively). As the temperature is lowered, $B^{\parallel}_{c2}$ initially increases steeply and then saturates. Increasing n_s causes a monotonic rise of $B^{\parallel}_{c2}$. This is already apparent in Fig. 3b, but even more so in the phase diagram plotted in Fig. 4 that includes numerous additional data points down to n_Q.

The behaviour of $B^{\parallel}_{c2}$ shown in Fig. 3 with an enhancement below the characteristic temperature $t_c T_{C0}$ is reminiscent of what frequently appears in layered superconductors[18,19,22,31] due to a transition from three-dimensional-like layer-coherent superconductivity to 2D-like layer decoupled superconductivity, when the out-of-plane coherence length, $\xi^{\perp}$, drops below the layer spacing as the temperature is lowered below the characteristic temperature T^*. In systems that undergo such a dimensional crossover, there inevitably exists a temperature window $T^* < T < T_{C0}$ in which $\xi^{\perp}$ is below the sample thickness and concomitantly exceeds the layer spacing. Josephson vortices, whose size is determined by $\xi^{\perp}$, can then penetrate the sample cross section. They force part of each superconducting layer into the normal state; however, due to vortex pinning, dissipationless transport persists. Under these circumstances, the loss of superconductivity is not governed by the orbital-effect limit as in our samples but rather the onset of Josephson vortex depinning, which requires a much larger in-plane field that depends linearly on temperature. This is illustrated for our sample IP-2 in Fig. 3c where the orbital-effect limit is compared with the required field for vortex depinning. Clearly, Josephson vortex depinning cannot be the cause for the loss of superconductivity at $T > t_c T_{C0}$ in our samples. In layered superconductors with a dimensional crossover, Josephson vortex depinning becomes irrelevant for $B^{\parallel}_{c2}$ when $\xi^{\perp}$ drops below the layer spacing when $T < T^*$. Josephson vortices now fit inside the layer spacing and each layer turns into a decoupled 2D superconductor. As a result, a spin-based pair-breaking mechanism will be responsible for the transition to the normal state. This causes the upturn in $B^{\parallel}_{c2}$. Despite the deceiving resemblance, this dimensional crossover scenario with

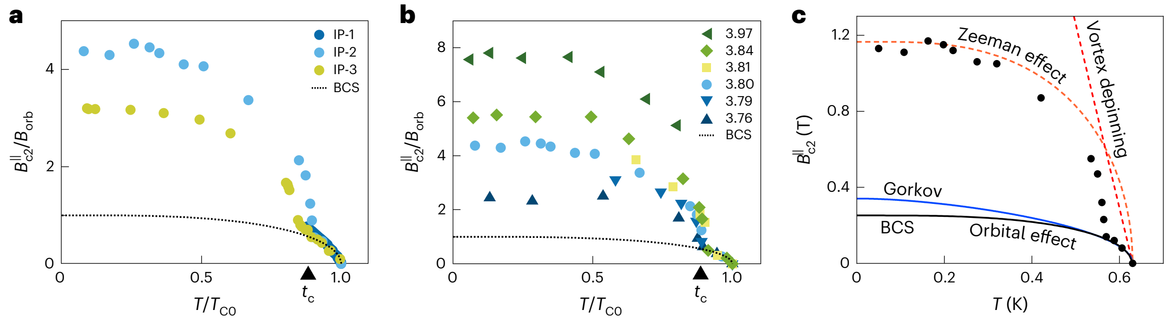

Fig. 3 | The variation of $B^{\parallel}_{c2}$ with temperature, density and critical temperature. a, Temperature dependence of $B^{\parallel}_{c2}$ for three different samples. The field is normalized to the zero-temperature orbital-effect limit. The T_{C0} of samples IP-1, IP-2 and IP-3 are 1.63 K, 0.63 K and 0.75 K respectively. Sample IP-1 was measured in a dry system with a base temperature of 1.5 K preventing the entry of the $t < t_c$ regime. **b**, Same as in **a** but data are recorded for sample IP-2 with various backgate voltages, establishing corresponding carrier densities labelled in units of 10^{13} cm^{-2} in the legend. T_{C0} varies from 380 to 820 mK for low to high density. The dotted lines in **a** and **b** mark the orbital-effect limit (equation (1)). **c**, Comparison of the experimentally observed temperature dependence of the in-plane upper critical field for sample IP-2 at zero backgate voltage with the orbital-effect limit determined from the BCS gap equation (black line) and Gorkov's linearized gap equation (blue line), as well as the BCS paramagnetic limit (orange dashed line) and the limit on superconductivity imposed by Josephson vortex depinning (red dashed line) (Supplementary Section 6).

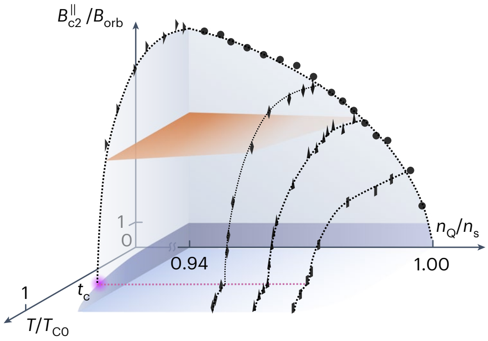

Fig. 4 | Phase diagram. Summary of all data recorded on sample IP-2 in the parameter space spanned by the normalized n_s, T and $B^{\parallel}$. The red-shaded plane marks the Pauli limit.

the transition of Josephson vortex depinning to spin-based pair breaking at its core is not applicable to our samples. Not only does vortex depinning play no role for $B^{\parallel}_{c2}$, for our samples $\xi^{\perp}$ exceeds the layer spacing and is comparable to the film thickness even at zero temperature (Fig. 2c). The assumption that $\xi^{\perp}$ would drop below the layer spacing for $T < t_c T_{c0}$ would also imply that the system must behave as two decoupled superconducting monolayers. This, as reported previously in the literature[20,23], would give rise to Ising superconductivity with a dramatically enhanced $B^{\parallel}_{c2}$ of several times the Pauli limit since monolayers no longer exhibit centrosymmetry, and the externally applied $B^{\parallel}$ has to compete with a large out-of-plane spin-orbit induced field; however, this contradicts the experimental data. For the data shown in Fig. 3a,b $B^{\parallel}_{c2}$ lies between $0.4B_P$ and $1.6B_P$ and is in most cases even smaller than the Pauli limit. We note that because of the preserved mirror symmetry in our geometry, Rashba SOC should not play a role. The larger layer separation, the reduced interlayer hopping and the improved quality in samples with intercalated lithium should all lead to a more pronounced rather than a suppressed Ising superconductivity. Clearly, the original assumption that a dimensional crossover occurs at $t_c T_{c0}$ cannot be supported. This argument is compelling, as it does not rely on any particular theoretical model for the extraction of $\xi^{\perp}$, or the description of $B^{\parallel}_{c2}$ such as the Klemm–Luther–Beasley theory[31]. This makes dimensional crossover physics obsolete. A more quantitative analysis can be found in Supplementary Section 6, and Supplementary Section 3 explains why disordered or two-band superconductivity can also be excluded.

Representation	Cooper pairing	Illustration
$A_{1g,1}$	$c_{\uparrow +}c_{\downarrow +} + c_{\uparrow -}c_{\downarrow -}$	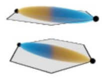
$A_{1g,2}$	$c_{\uparrow +}c_{\downarrow -} + c_{\uparrow -}c_{\downarrow +}$	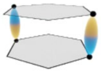
A_{1u}	$c_{\uparrow +}c_{\downarrow +} - c_{\uparrow -}c_{\downarrow -}$	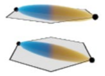
A_{2u}	$c_{\uparrow +}c_{\downarrow -} - c_{\uparrow -}c_{\downarrow +}$	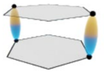
E_u	$c_{\uparrow +}c_{\uparrow -}$, $c_{\downarrow +}c_{\downarrow -}$	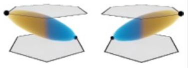

Fig. 5 | Symmetry-allowed intralayer and interlayer pairing channels for *s*-wave superconductivity in a 2H-MoS$_2$ bilayer. The arrows denote the spin and ± the layer index. The phase of the Cooper-pair wave functions is schematically indicated by colours.

The data are here discussed in the context of the pairing scheme proposed in ref. 12. We will follow this theory closely, but omit some details that may be obtained from the reference. The experimentally established layer coherence in our samples dictates that the gap function inherits the global symmetry of the bilayer and contains contributions from independent pairing channels assigned to the irreducible representations of the D_{3d} symmetry group. For *s*-wave superconductivity, all symmetry-allowed pairing channels are listed in Fig. 5. Among these, the intralayer pairing channels $A_{1g,1}$ and A_{1u} were identified as energetically more favourable. Because $B^{\parallel}$ perturbs the D_{3d} symmetry, these two channels can hybridize. This generates an additional term in the free energy of the superconducting state of the form $K(B^{\parallel}, q, t_{\perp}, \beta_{SOC})\Delta^{*}_{A_{1g,1}}\Delta_{A_{1u}} + c.c.$ with K being the off-diagonal coefficient, describing the mixing between the two channels, and *c.c.* denoting the complex conjugate. This term depends on $B^{\parallel}$, the Cooper-pair centre-of-mass momentum q, the interlayer hopping $t_{\perp}$ and the strength of the SOC β_{SOC} that is responsible for spin-valley locking and Ising superconductivity in the monolayer regime.

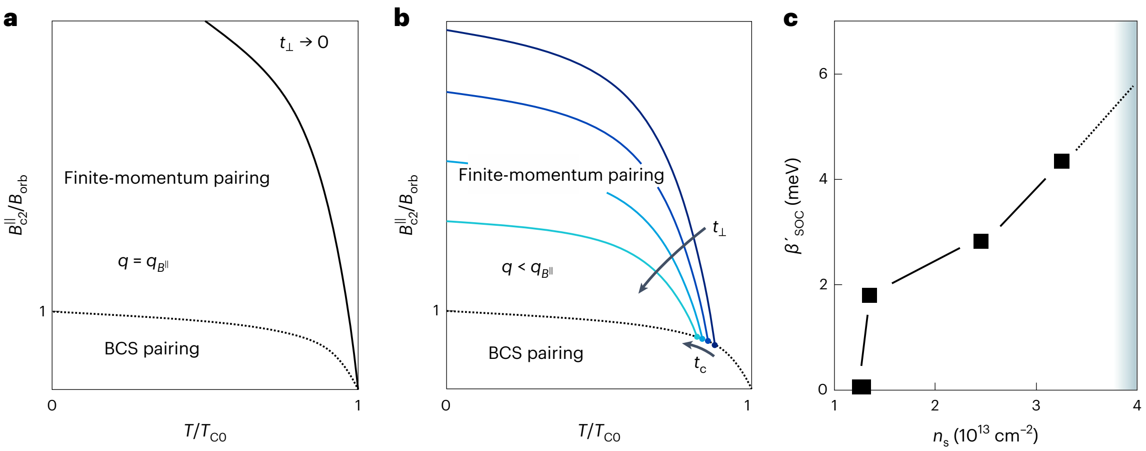

Fig. 6 | Resilience of the superconducting state composed of Cooper pairs with non-zero momentum against an in-plane magnetic field. a, Schematic diagram of the in-plane upper critical field as a function of temperature as $t_\perp \to 0$. The dotted line marks the orbital-effect limit. **b**, Same as in **a** but for non-vanishing, increasing $t_\perp$. A tricritical point appears in the diagram and shifts towards lower temperature in accordance with equation (2) with increasing $t_\perp$. The upper critical field gets reduced with increasing $t_\perp$ because the portion of the Fermi surfaces that can participate in pairing shrinks with increasing $t_\perp$. **c**, Total SOC strength β'_{SOC} as a function of density n_s obtained from a study of quantum corrections to the conductivity in samples with densities below n_Q that remain metallic. The grey shaded region marks the carrier density range covered with sample IP-2.

The complex gap functions $\Delta_{A_{1g,1}}$ and $\Delta_{A_{1u}}$ are associated with both pairing channels. Under certain circumstances, the free energy does not reach its minimum at $q = 0$ but at $q = q_m \neq 0$ turning finite-momentum pairing energetically advantageous. Here, q_m is the momentum for which the free energy reaches its minimum. The critical temperatures of the $A_{1g,1}$ and A_{1u} channels depend on β_{SOC} and $t_\perp$. For the case of $t_\perp \to 0$, these temperatures are identical and both pairing channels can always coexist. If $B^\parallel/B_{orb} < \tanh 1.74\sqrt{T_{C0}/T - 1}$, the free energy exhibits a minimum at $q_m = 0$, and the energy difference of paired electrons resulting from the orbital effect is smaller than the BCS gap amplitude. For larger in-plane fields such that $B^\parallel/B_{orb} > \tanh 1.74\sqrt{T_{C0}/T - 1}$ the minimum occurs at twice the field-induced shift experienced by the two Fermi surfaces at the K and K' symmetry points, $|q_m| = 2|\mathbf{q}_{B^\parallel}| = edB^\parallel/\hbar$ (cf. Fig. 1b), resulting in the schematic diagram plotted in Fig. 6a. The orbital effect is no longer the pair-breaking limit, because the energy difference of the electrons participating in the pairing is eliminated by adopting a non-zero centre-of-mass momentum $\hbar\mathbf{q}_m$ and hence superconductivity persists up to higher fields. As q_m turns non-zero, the gap transits to $\Delta(\mathbf{r}) = \Delta_+ e^{i\mathbf{q}_m\cdot\mathbf{r}} + \Delta_- e^{-i\mathbf{q}_m\cdot\mathbf{r}}$ where $\Delta_\pm$ are degenerate linear combinations of $\Delta_{A_{1g,1}}$ and $\Delta_{A_{1u}}$. Note that for $|q_m| = 2|\mathbf{q}_{B^\parallel}|$, the full Fermi surfaces can participate in pairing. In the more realistic case of non-zero $t_\perp$, the critical temperature of the pairing channels are distinct and in particular, $T_{C0,A_{1g,1}} = T_{C0} > T_{C0,A_{1u}}$. This introduces a tricritical point t_c in the phase diagram (Fig. 6b) with

$$t_c = \frac{T_{C0,A_{1u}}}{T_{C0,A_{1g,1}}} = \exp\left[-\frac{(t_\perp/\beta_{SOC})^2}{2N_0U_0}\right] \quad (2)$$

where N_0 is the density of states at the Fermi surface and $2U_0$ is the pairing interaction for $A_{1g,1}$. For $T_{C0,A_{1g,1}} > T > T_{C0,A_{1u}}$, only the $A_{1g,1}$ channel contributes to the gap, the BCS state of Cooper pairs with zero centre-of-mass momentum and a uniform gap $\Delta = \Delta_{A_{1g,1}}$ is favoured. In this regime, superconductivity is quenched by the orbital effect and $B^\parallel_{c2}$ follows equation (1) in agreement with the experimental results; however, for $T < T_{C0,A_{1u}}$, that is, $T/T_{C0} < t_c$, both pairing channels coexist. Finite-momentum pairing returns and raises $B^\parallel_{c2}$ with a sharp upturn near t_c. This qualitatively fits the experimental results.

Larger interlayer hopping is detrimental for finite-momentum pairing. It not only reduces t_c but also shifts $|q_m|$ to values lower than $2|\mathbf{q}_{B^\parallel}|$. As a result, on some parts of the Fermi surfaces, potential electron pairs will not associate due to too large an energy difference. This is similar to the FFLO state where only some segments of Fermi surfaces participate in pairing. This reduces the pairing stability. It presumably is not a coincidence that this finite-momentum pairing is discovered here in MoS_2 in view of its weak interlayer hopping[29,32,33]. It is possible to estimate $t_\perp$ from the experimentally observed value of t_c and equation (2). The electron-phonon coupling strength and the average phonon energy[34–36] yield $N_0U_0 \approx 0.1$ for sample IP-2 with T_{C0} = 630 mK. While we are unaware of an experimental method to extract β_{SOC} in equation (2) directly, β_{SOC} together with $t_\perp$ accounts for the total spin splitting between opposite spin states: $2\beta'_{SOC} = 2\sqrt{\beta^2_{SOC} + t^2_\perp}$. This β'_{SOC} can be extracted from quantum corrections to the conductivity for samples in the normal state (Supplementary Section 7). Data points are plotted in Fig. 6c, and the behaviour can be extrapolated to densities larger than n_Q where samples exhibit superconductivity. In that density regime, β'_{SOC} is estimated to be about 5 meV. Together with $t_c = 0.9$ this yields a $t_\perp$ of about 0.7 meV. This is more than an order of magnitude smaller than the reported values for $NbSe_2$ and TaS_2 (refs. 20,21). For double-side gated MoS_2 bilayers[22], larger values of $t_\perp$ of a few meV have been reported, presumably as a result of additional scattering-assisted hopping. The small value of $t_\perp$ also implies that t_c only weakly depends on β'_{SOC}, consistent with the experimental observation of a nearly fixed t_c across the density range we were able to explore. Qualitatively, the larger enhancement of $B^\parallel_{c2}$ with increasing density by tuning the backgate in Fig. 3b,c can also be understood, since the relative importance of $t_\perp$ for β'_{SOC} diminishes and $|q_m|$ approaches $2|\mathbf{q}_{B^\parallel}|$, such that a larger portion of the Fermi surface can participate in pairing.

By using remote lithium intercalation as a doping technique, it has been possible to preserve the centrosymmetry of a MoS_2 bilayer and boost $\xi^\perp$ such that both layers remain coherent down to zero temperature. These are key prerequisites for the observation of the orbital-effect-based instance of finite-momentum pairing put forward in ref. 12. The behaviour of $B^\parallel_{c2}$ is consistent with this pairing scheme, in particular because of the importance of the BCS orbital-effect limit and the absence of Josephson vortex depinning in the upper temperature range of superconductivity, and even more so the lack of Ising superconductivity in the lower temperature regime. Other proposed unconventional pairing mechanisms also do not match with our data (Supplementary Sections 3, 6 and 8).

Online content

Any methods, additional references, Nature Portfolio reporting summaries, source data, extended data, supplementary information, acknowledgements, peer review information; details of author contributions and competing interests; and statements of data and code availability are available at https://doi.org/10.1038/s41567-023-02202-4.

References

1. Fulde, P. & Ferrell, R. A. Superconductivity in a strong spin-exchange field. *Phys. Rev.* **135**, A550 (1964).
2. Larkin, A. & Ovchinnikov, Y. N. Nonuniform state of superconductors. *Sov. Phys. JETP-USSR* **20**, 762–770 (1965).
3. Uji, S. et al. Vortex dynamics and the Fulde-Ferrell-Larkin-Ovchinnikov state in a magnetic-field-induced organic superconductor. *Phys. Rev. Lett.* **97**, 157001 (2006).
4. Lortz, R. et al. Calorimetric evidence for a Fulde-Ferrell-Larkin-Ovchinnikov superconducting state in the layered organic superconductor κ-(BEDT-TTF)$_2$Cu(NCS)$_2$. *Phys. Rev. Lett.* **99**, 187002 (2007).
5. Mayaffre, H. et al. Evidence of Andreev bound states as a hallmark of the FFLO phase in κ-(BEDT-TTF)$_2$Cu(NCS)$_2$. *Nat. Phys.* **10**, 928–932 (2014).
6. Kaur, R. P., Agterberg, D. F. & Sigrist, M. Helical vortex phase in the noncentrosymmetric CePt$_3$Si. *Phys. Rev. Lett.* **94**, 137002 (2005).
7. Mironov, S. & Buzdin, A. Spontaneous currents in superconducting systems with strong spin-orbit coupling. *Phys. Rev. Lett.* **118**, 077001 (2017).
8. Kenzelmann, M. et al. Coupled superconducting and magnetic order in CeCoIn$_5$. *Science* **321**, 1652–1654 (2008).
9. Kim, D. Y. et al. Intertwined orders in heavy-fermion superconductor CeCoIn$_5$. *Phys. Rev. X* **6**, 041059 (2016).
10. Edkins, S. D. et al. Magnetic field-induced pair density wave state in the cuprate vortex halo. *Science* **364**, 976–980 (2019).
11. Liu, X., Chong, Y. X., Sharma, R. & Davis, J. S. Discovery of a Cooper-pair density wave state in a transition-metal dichalcogenide. *Science* **372**, 1447–1452 (2021).
12. Liu, C.-X. Unconventional superconductivity in bilayer transition metal dichalcogenides. *Phys. Rev. Lett.* **118**, 087001 (2017).
13. Xu, X., Yao, W., Xiao, D. & Heinz, T. F. Spin and pseudospins in layered transition metal dichalcogenides. *Nat. Phys.* **10**, 343–350 (2014).
14. Zhang, X., Liu, Q., Luo, J.-W., Freeman, A. J. & Zunger, A. Hidden spin polarization in inversion-symmetric bulk crystals. *Nat. Phys.* **10**, 387–393 (2014).
15. Brotons-Gisbert, M. et al. Spin-layer locking of interlayer excitons trapped in moiré potentials. *Nat. Mater.* **19**, 630–636 (2020).
16. Schmidt, V. V. *The Physics of Superconductors: Introduction to Fundamentals and Applications* (Springer Science & Business Media, 2013).
17. Tinkham, M. *Introduction to Superconductivity* (Courier Corporation, 2004).
18. Woollam, J. A. & Somoano, R. B. Superconducting critical fields of alkali and alkaline-earth intercalates of MoS$_2$. *Phys. Rev. B* **13**, 3843 (1976).
19. Coleman, R. V., Eiserman, G. K., Hillenius, S. J., Mitchell, A. T. & Vicent, J. L. Dimensional crossover in the superconducting intercalated layer compound 2H-TaS$_2$. *Phys. Rev. B* **27**, 125 (1983).
20. Xi, X. et al. Ising pairing in superconducting NbSe$_2$ atomic layers. *Nat. Phys.* **12**, 139–143 (2016).
21. de la Barrera, S. C. et al. Tuning Ising superconductivity with layer and spin-orbit coupling in two-dimensional transition-metal dichalcogenides. *Nat. Commun.* **9**, 1427 (2018).
22. Zheliuk, O. et al. Josephson coupled Ising pairing induced in suspended MoS$_2$ bilayers by double-side ionic gating. *Nat. Nanotechnol.* **14**, 1123–1128 (2019).
23. Lu, J. M. et al. Evidence for two-dimensional Ising superconductivity in gated MoS$_2$. *Science* **350**, 1353–1357 (2015).
24. Saito, Y. et al. Superconductivity protected by spin-valley locking in ion-gated MoS$_2$. *Nat. Phys* **12**, 144–149 (2016).
25. Kühne, M. et al. Ultrafast lithium diffusion in bilayer graphene. *Nat. Nanotechnol.* **12**, 895–900 (2017).
26. Kühne, M. et al. Reversible superdense ordering of lithium between two graphene sheets. *Nature* **564**, 234–239 (2018).
27. Beasley, M. R., Mooij, J. E. & Orlando, T. P. Possibility of vortex-antivortex pair dissociation in two-dimensional superconductors. *Phys. Rev. Lett.* **42**, 1165 (1979).
28. Ye, J. T. et al. Superconducting dome in a gate-tuned band insulator. *Science* **338**, 1193–1196 (2012).
29. Nakamura, Y. & Yanase, Y. Odd-parity superconductivity in bilayer transition metal dichalcogenides. *Phys. Rev. B* **96**, 054501 (2017).
30. Watanabe, T., Yoshida, T. & Yanase, Y. Odd-parity superconductivity by competing spin-orbit coupling and orbital effect in artificial heterostructures. *Phys. Rev. B* **92**, 174502 (2015).
31. Klemm, R. A., Luther, A. & Beasley, M. R. Theory of the upper critical field in layered superconductors. *Phys. Rev. B* **12**, 877 (1975).
32. Razzoli, E. et al. Selective probing of hidden spin-polarized states in inversion-symmetric bulk MoS$_2$. *Phys. Rev. Lett.* **118**, 086402 (2017).
33. Pisoni, R. et al. Absence of interlayer tunnel coupling of K-valley electrons in bilayer MoS$_2$. *Phys. Rev. Lett.* **123**, 117702 (2019).
34. McMillan, W. L. Transition temperature of strong-coupled superconductors. *Phys. Rev.* **167**, 331 (1968).
35. Allen, P. B. & Dynes, R. C. Transition temperature of strong-coupled superconductors reanalyzed. *Phys. Rev. B* **12**, 905 (1975).
36. Das, T. & Dolui, K. Superconducting dome in MoS$_2$ and TiSe$_2$ generated by quasiparticle-phonon coupling. *Phys. Rev. B* **91**, 094510 (2015).

Publisher's note Springer Nature remains neutral with regard to jurisdictional claims in published maps and institutional affiliations.

Open Access This article is licensed under a Creative Commons Attribution 4.0 International License, which permits use, sharing, adaptation, distribution and reproduction in any medium or format, as long as you give appropriate credit to the original author(s) and the source, provide a link to the Creative Commons license, and indicate if changes were made. The images or other third party material in this article are included in the article's Creative Commons license, unless indicated otherwise in a credit line to the material. If material is not included in the article's Creative Commons license and your intended use is not permitted by statutory regulation or exceeds the permitted use, you will need to obtain permission directly from the copyright holder. To view a copy of this license, visit http://creativecommons.org/licenses/by/4.0/.

© The Author(s) 2023

Methods

Device fabrication

MoS_2 bilayers were mechanically exfoliated from bulk crystals (HQ Graphene) onto polydimethylosiloxane-based elastomeric films (Gel-Pak) using adhesive tape. These were then transferred onto a heavily P-doped Si-substrate covered with a 300 nm thick dry thermal SiO_2. To remove residual glue and release strain, the substrate with sample was placed in a furnace and thermally annealed in a forming gas atmosphere (300 °C, 145 mbar) for 10 minutes. The MoS_2 bilayers were then shaped into a Hall bar geometry with the help of electron-beam lithography and a CHF_3/O_2-plasma reactive-ion etch. The Hall bar geometry is designed such that the centre-to-centre distance between adjacent voltage probes along the perimeter is 1.75 times the width of the sample. We will refer to this ratio as the aspect ratio. Voltage probes, source and drain contact leads and a counter-electrode for a galvanic cell were made out of Ti using electron-beam lithography, thermal evaporation and lift-off. A graphene multilayer was then placed on top of the MoS_2 bilayer to cover only a small portion of its boundary. Subsequently, the device was moved into an argon-filled glovebox. A small piece of lithium metal was daubed onto the counter-electrode, so it could serve as a lithium reservoir and reference for the electrochemical potential. The polymer electrolyte was drop-cast to form a galvanic cell by covering the lithium metal and part of the edge of the graphene multilayer. The electrolyte was composed of 0.35 M lithium bis(trifluoromethane) sulfonimide dissolved in a 3:7 w/w mixture of polyethylene glycol methyl ether methacrylate and bisphenol A ethoxylate dimethacrylate with 2–4 wt% of 2-hydroxy-2-methylpropiophenone as a photoinitiator. This peripheral galvanic cell has been deployed previously for the study of lithium diffusion using Hall voltammetry[25] and lithium crystal formation using transmission electron microscopy in bilayer graphene[26]. A schematic illustration of the device geometry is shown in Fig. 1c. Optical images of some devices are shown in the insets of Extended Data Fig. 1 and Supplementary Figs. 2–4 and 7.

Galvanostatic intercalation

Galvanostatic intercalation of lithium was initiated by driving a constant d.c. current (typically 0.5 pA) from the counter-electrode of the galvanic cell to the drain electrode on the MoS_2 bilayer and monitoring the potential of MoS_2 against lithium with the help of a source measure unit (Keithley 237). Lithium enters the van der Waals galleries through defects or at the boundary of the graphene multilayer, where it is covered by the electrolyte drop. Diffusive forces then tend to homogeneously spread the lithium across the entire sample. The lithium filled graphene multilayer acts as a solid state lithium source for lithium uptake into the MoS_2 bilayer. This arrangement, where the graphene multilayer acts as a conveyor to bring lithium from the electrolyte drop to the MoS_2 bilayer, offers multiple advantages. The MoS_2 remains entirely undisturbed from liquid coverage and this 'conveyor belt'-method is applicable to flakes with small footprint. The electrolyte and electrolyte composition of the galvanic cell were optimized in a tedious process for multilayer graphene[37]. The gathered expertise can be deployed in subsequent research, and reoptimization can be avoided in applications to other 2D materials, such as MoS_2.

To verify charge transfer to the MoS_2 layers from lithium intercalants, the longitudinal resistivity is monitored in a four terminal configuration. To this end, an additional a.c. current was imposed through the source and drain contacts of the MoS_2 bilayer with a 1 V_{rms} sinusoidal voltage source and a 10 MΩ resistor in series. The current flowing between the source and drain contacts and the voltage across a pair of voltage probes along the Hall bar perimeter are measured simultaneously with lock-in amplifiers. The sheet resistance is calculated from the measured longitudinal resistance by division of the latter with the aspect ratio. After the first lithiation cycle, the sample was illuminated with ultraviolet light to cure and solidify the polymer electrolyte drop.

Magnetotransport measurements

Transport measurements were carried out in a cryogen-free superconducting magnet system or a top-loading-into-mixture dilution refrigerator. Measurements in the cryogen-free system involved an undesirable exposure of the sample to air for about one minute, but offered a wider accessible range of sample temperature ($\lesssim$1.5 K to 300 K). The sample holder for the top-loading-into-mixture dilution refrigerator is equipped with a sliding seal and was modified with a valve arrangement to enable sample mounting within the glovebox and a transfer to the dilution refrigerator with no exposure to ambient air. To improve the carrier density homogeneity, multiple delithiation and relithiation cycles were run at 300 K after mounting the sample rod on the dilution refrigerator cryostat. During sample loading, special care was taken to avoid low pressure of the sample space while the temperature was still above ~250 K. Ions are still mobile at this temperature and unintended progressive delithiation was observed when evacuating the sample space. This may be related to outgassing of the electrolyte drop. Four terminal longitudinal resistivity and Hall resistivity measurements were performed by driving an a.c. current with an amplitude of 100 nA_{rms} and a frequency of 17.77 Hz between the source and drain contacts and recording the Hall and longitudinal voltage drops with lock-in amplifiers. The four terminal d.c. current-voltage characteristics were acquired with a source measure unit (KEI237, Keithley Instruments) in series with a 1 MΩ resistor, a voltage amplifier (SR560, Stanford Research) and a precision multimeter (34401A, Agilent).

In this work a total of 11 samples were investigated with different levels of intercalation, that is, carrier densities. Five of these samples belonged to the underdoped regime; in them, the carrier density was below the quantum critical point density n_Q for superconductivity and these samples behaved metallic down to the lowest temperatures. They are labelled as M-1 to M-5. The six remaining samples with densities above n_Q exhibited superconductivity and were mounted for out-of-plane magnetic field studies (samples OP-1 to OP-3) or for in-plane magnetic field studies (samples IP-1 to IP-3).

Data availability

Source data are provided with this paper.

References

37. Kühne, M. et al. Wettability engineering for studying ion transport in 2D layered materials. *Adv. Mater. Interfaces* **8**, 2001453 (2021).

Acknowledgements

We thank E. König and P. Ostrovsky for discussions and S. Wahl for technical support. J.S. acknowledges financial support from the EU Graphene Flagship Core 3 Project and the SPP 2244 project of the DFG.

Author contributions

J.S. conceived the experiments and concepts. D.Z. conducted the experiments and analysis. D.Z., L.D., M.K., S.F., N.G. and J.S. discussed the work. J.S. supervised the work. D.Z. and J.S. wrote the paper.

Funding

Open access funding provided by Max Planck Society.

Competing interests

The authors declare no competing interests.

Additional information

Extended data is available for this paper at https://doi.org/10.1038/s41567-023-02202-4.

Supplementary information The online version contains supplementary material available at https://doi.org/10.1038/s41567-023-02202-4.

Correspondence and requests for materials should be addressed to Jurgen Smet.

Peer review information *Nature Physics* thanks Yong Xu and the other, anonymous, reviewer(s) for their contribution to the peer review of this work.

Reprints and permissions information is available at www.nature.com/reprints.

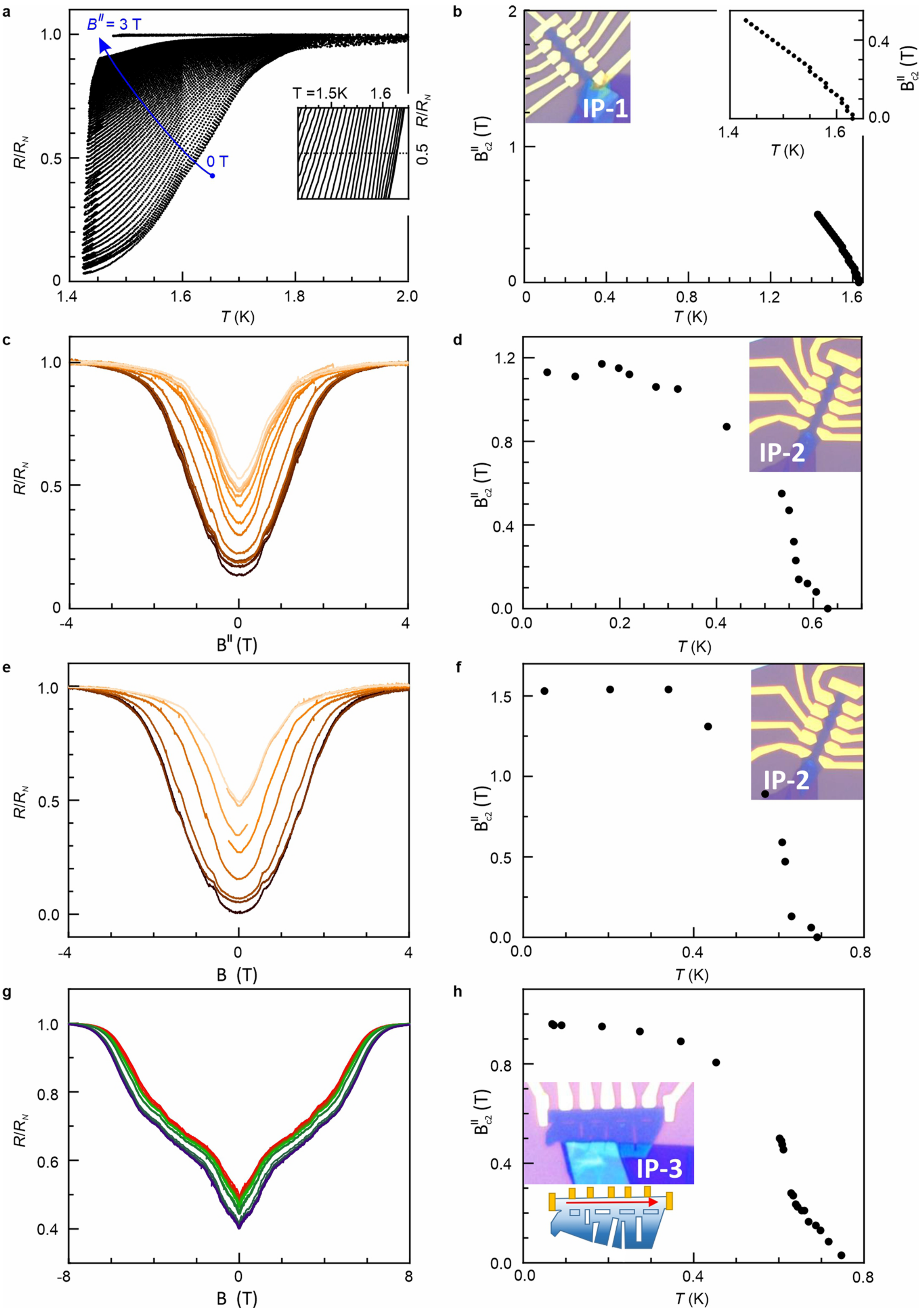

Extended Data Fig. 1 | Determination of the in-plane upper critical field for samples IP-1, IP-2 and IP-3. a, R–T curves at various in-plane magnetic fields recorded on sample IP-1. The inset is a zoom near half of the normal-state resistance, defined as the boundary between the superconducting and normal state. **b**, Temperature dependence of the in-plane upper critical field for sample IP-1 extracted from the data set presented in panel (a). **c**, **e**, Magnetoresistance recorded on sample IP-2 for two backgate voltages and with temperature as an additional parameter: Panel (c) 0 V, 50 mK < T < 650 mK; Panel (e) 13 V, 50 mK < T < 676 mK. **d**, **f**, Temperature dependence of the in-plane upper critical field for Sample IP-2 extracted from the data sets in panel (c) and (e), respectively. **g**, Magnetoresistance recorded on sample IP-3 for various temperatures (68 mK < T < 747 mK). **h**, Temperature dependence of the in-plane upper critical field extracted from the data set in panel (g).